Hindawi Publishing Corporation
Mathematical Problems in Engineering
Volume 2014, Article ID 548708, 13 pages
http://dx.doi.org/10.1155/2014/548708

Research Article

Geometric Nonlinear Meshless Analysis of Ribbed Rectangular Plates Based on the FSDT and the Moving Least-Squares Approximation

L. X. Peng,[1,2] Yue-Ping Tao,[3] Hong-Qiao Li,[1,2] and Gui-Kai Mo[1]

[1] *College of Civil Engineering and Architecture, Guangxi University, Nanning 530004, China*
[2] *Guangxi Key Laboratory of Disaster Prevention and Engineering Safety, Guangxi University, Nanning 530004, China*
[3] *Guangxi Polytechnic of Construction, Nanning 530003, China*

Correspondence should be addressed to L. X. Peng; penglx@gxu.edu.cn

Received 17 December 2013; Revised 14 January 2014; Accepted 21 January 2014; Published 13 March 2014

Academic Editor: Yumin Cheng

Based on the first-order shear deformation theory (FSDT) and the moving least-squares approximation, a new meshless model to study the geometric nonlinear problem of ribbed rectangular plates is presented. Considering the plate and the ribs separately, the displacement field, the stress, and strain of the plate and the ribs are obtained according to the moving least-squares approximation, the von Karman large deflection theory, and the FSDT. The ribs are attached to the plate by considering the displacement compatible condition along the connections between the ribs and the plate. The virtual strain energy formulation of the plate and the ribs is derived separately, and the nonlinear equilibrium equation of the entire ribbed plate is given by the virtual work principle. In the new meshless model for ribbed plates, there is no limitation to the rib position; for example, the ribs need not to be placed along the mesh lines of the plate as they need to be in FEM, and the change of rib positions will not lead to remeshing of the plate. The proposed model is compared with the FEM models from pieces of literature and ANSYS in several numerical examples, which proves the accuracy of the model.

1. Introduction

Ribbed plate has been widely used in engineering, such as bridges, ship hulls, and aviation, and it is a popular structure with obvious advantages. The ribs make the structure stiffer and allow it to achieve larger bearing capacity than flat plate with roughly the same weight. However, the ribs also bring difficulties to analysis, and the calculation of ribbed plate is more complicated than that of flat plates. Based on the fact that the ribs of many ribbed plates are attached to the plate with uniform spacing and close to one another, and that ribbed plates show different elastic characteristics in the two perpendicular directions, early researchers transformed the ribs to an addition layer to the plate and used the orthotropic model to approximate the ribbed plates [1]. Another early model was the grillage model [2]. The models were simple and fulfilled the demand of fast and easy computation in engineering. Therefore, they are still used in some design environments, where accurate analysis is not the first concern. However, because the models were introduced in the age of lacking computational tools and some approximations were adopted, they cannot give satisfying results in solving generalized ribbed plate problems. Due to the advances of computers and numerical methods in the past decades, a ribbed plate model which has more universality was introduced, regarding the ribbed plate as a composite structure of ribs and plate and analyzing them separately; combining them by imposing the displacement compatibility conditions between them, this is also the model which is accepted widely. Several methods have been developed, such as the Rayleigh-Ritz method [3–7] and the finite element methods (FEM) [8, 9].

Not many nonlinear analyses of ribbed plates can be found in pieces of literature, and most of them were based on the FEM [10–13], which benefits from the good adaptability and high accuracy of the method. However, no method is

perfect, and FEMs also have disadvantages. The FEMs rely on the meshes that discretize problem domain to construct their approximated solution, but the large deformation of problem domain always leads to mesh disorder, and, therefore, time-consuming and accuracy-suffering remeshing is unavoidable, which brings difficulties to both programming and analysis. And for ribbed plate problems, most FEMs require that the ribs are placed along the mesh lines and any change in their positions will lead to the remeshing of the plate domain to accommodate the change. If the layout of ribs needs to be optimized, there may be hundreds of times of remeshing before obtaining the ideal result. And if the optimization is carried out under the consideration of the large deformation of a ribbed plate, the number of remeshing may become a dramatic figure combing the iteration from the nonlinear analysis. Meshless or meshfree method [14–19] is a numerical method which bases their approximated solution entirely on a set of nodes distributed in a problem domain. Without a mesh, the meshless methods overcome the aforementioned difficulties that FEM encountered with the meshes. The moving least-squares approximation originated in data fitting. Nayroles et al. [14] were the first to use a moving least-squares procedure to develop a meshless approximation. By introducing moving least-squares interpolants to construct the trial and test functions for the variation principle (weak form), Belytschko et al. [15] improved the method proposed by Nayroles et al. [14] and proposed the element-free Galerkin method (EFG). Nevertheless, due to the fact that the shape function of most meshless methods lacks Kronecker delta properties, and that the unknowns of the governing equation are nodal parameters other than nodal displacements, the displacement compatible conditions between the components of a composite structure cannot be implemented directly in meshless methods as they can in FEMs when the structure is analyzed, which limits the application of meshless methods in engineering. Recently, the analysis of plate and composite structure with meshless methods has made some progress. Lei et al. [20, 21] analyzed buckling and large deformation of functionally graded plate using the element-free kp-Ritz method. Zhang et al. [22] used a local Kriging meshless method to study the thermal buckling of functionally graded plates. The author Peng and his coworkers have proposed meshless methods to solve the linear bending, free vibration, and elastic buckling problems of ribbed plates with a derived transformation equation to address the nodal parameter issue [23, 24]. However, the equation did not consider all necessary displacement compatible conditions, which leads to failure in solving the large deformation problem of ribbed plates. The objective of this paper is to propose a meshless model to study the geometric nonlinear behaviors of ribbed plates from the perspective of composite structure. Based on the first-order shear deformation theory (FSDT), the moving least-squares approximation (MLS) and von Karman's large deflection theory, the displacement field, nonlinear strains, and nonlinear equilibrium equations of the plate and ribs are derived. A new equation that transforms the nodal parameters of the ribs to those of the plate is introduced, and the equation allows the displacement compatible condition between the plate and the ribs to be implemented directly. Because of the meshless characteristics of the proposed model, the ribs need not to be placed along the mesh lines of the plate, and the change of rib positions will not lead to remeshing of the plate. Mesh disorder due to the large deformation of problem domain is avoided, as well. Some numerical examples are utilized to demonstrate the accuracy of the proposed model. The calculated results are compared with the results from ANSYS and pieces of literature. The proposed meshless model of ribbed plate can provide a substantial ground for future optimization of rib layout under the consideration of large deformation.

2. Moving Least-Squares Approximation

In MLS [15], a function $v(x)$ defined in a domain Ω can be approximated by $v^h(x)$ in the subdomain $\Omega_{\mathbf{x}}$. $v^h(x)$ is defined as

$$v^h(\mathbf{x}) = \sum_{i=1}^{m} q_i(\mathbf{x})\, b_i(\mathbf{x}) = \mathbf{q}^{\mathbf{T}}(\mathbf{x})\, \mathbf{b}(\mathbf{x}), \tag{1}$$

where $q_i(\mathbf{x})$ are the monomial basis functions, h is a factor that measures the domain of influence of the nodes, m is the number of basis function, and $b_i(\mathbf{x})$ are their coefficients. In this paper, the quadratic basis $\mathbf{q}^{\mathbf{T}} = [1, x, x^2]$ ($m = 3$, in 1D); $\mathbf{q}^{\mathbf{T}} = [1, x, y, x^2, xy, y^2]$ ($m = 6$, in 2D) are used for the ribs and plates, respectively. The unknown coefficients $b_i(\mathbf{x})$ can be determined by minimizing a weighted discrete L_2 norm

$$\begin{aligned}\Gamma &= \sum_{I=1}^{N} \omega(\mathbf{x} - \mathbf{x}_I)\left[v^h(\mathbf{x}) - v_I\right]^2 \\ &= \sum_{I=1}^{N} \omega(\mathbf{x} - \mathbf{x}_I)\left[\mathbf{q}(\mathbf{x}_I)^{\mathbf{T}}\mathbf{b}(\mathbf{x}) - v_I\right]^2,\end{aligned} \tag{2}$$

where $\omega(\mathbf{x} - \mathbf{x}_I)$ or $\omega_I(\mathbf{x})$ is the weight function, $\omega_I(\mathbf{x}) = 0$ outside $\Omega_{\mathbf{x}}$, n is the number of nodes in $\Omega_{\mathbf{x}}$ that makes the weight function $\omega_I(\mathbf{x}) > 0$, and v_I are the nodal parameters. Minimizing Γ with respect to $\mathbf{b}(\mathbf{x})$,

$$\frac{\partial \Gamma}{\partial \mathbf{b}(\mathbf{x})} = 0, \tag{3}$$

we obtain

$$\mathbf{b}(\mathbf{x}) = \mathbf{A}^{-1}(\mathbf{x})\, \mathbf{B}(\mathbf{x})\, v, \tag{4}$$

where

$$\begin{aligned}\mathbf{B}(\mathbf{x}) &= \sum_{I=1}^{n} \omega(\mathbf{x} - \mathbf{x}_I)\, \mathbf{q}(\mathbf{x}_I)\, \mathbf{q}^{\mathbf{T}}(\mathbf{x}_I), \\ \mathbf{A}(\mathbf{x}) &= \left[\omega(\mathbf{x} - \mathbf{x}_1)\, q(\mathbf{x}_1), \omega(\mathbf{x} - \mathbf{x}_2)\, \mathbf{q}(\mathbf{x}_2),\right. \\ &\quad \left. \ldots, \omega(\mathbf{x} - \mathbf{x}_n)\, \mathbf{q}(\mathbf{x}_n)\right].\end{aligned} \tag{5}$$

Therefore, (1) can be expressed in a standard form as

$$u^h(\mathbf{x}) = \sum_{I=1}^{n} N_I(\mathbf{x})\, v_I, \tag{6}$$

where $N_I(\mathbf{x}) = \mathbf{q}^{\mathbf{T}}(\mathbf{x})\mathbf{B}^{-1}(\mathbf{x})\mathbf{A}_I(\mathbf{x})$ are the shape functions.

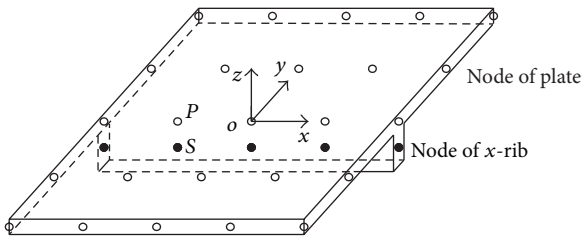

Figure 1: Meshless model of a ribbed plate.

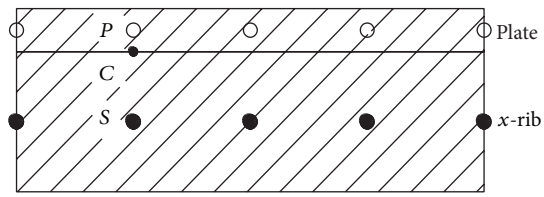

Figure 2: Section of plate and x-rib.

3. Meshless Model of a Ribbed Plate

The meshless model of a ribbed plate, shown in Figure 1, is composed of a plate and an x-rib. The plate and the rib are discretized by a set of nodes. The degree of freedom (DOF) of every node of plate is $(u_{0p}, v_{0p}, w_p, \varphi_{px}, \varphi_{py})$, where u_{0p}, v_{0p}, and w_p are the nodal translations of the plate in x, y, and z directions, respectively. φ_{px} and φ_{py} are the rotation about the y-axis and the x-axis, respectively. The DOF of every node of x-rib is $(u_{0sx}, w_{sx}, \varphi_{sx})$. The rib is assumed to be made from the same material as the plate. The Young's modulus is E and the Poisson's ratio is μ. If there is a y-rib, we can derive similar equations for y-rib as those for the x-rib.

3.1. Displacement Field Approximation of a Ribbed Plate. Based on the FSDT [25, 26], the displacement field of a plate is given as

$$\begin{aligned} u_p(x,y,z) &= u_{0p}(x,y) - z\varphi_{px}(x,y), \\ v_p(x,y,z) &= v_{0p}(x,y) - z\varphi_{py}(x,y), \\ w_p(x,y) &= w_p(x,y). \end{aligned} \tag{7}$$

According to the MLS approximation, the functions $u_{0p}(x, y), v_{0p}(x, y), w_p(x, y), \varphi_{px}(x, y)$, and $\varphi_{py}(x, y)$ can be expressed in a discrete form

$$\begin{aligned} u_p(x,y,z) &= \sum_{I=1}^{n} N_I(x,y)\, u_{0pI} - z\sum_{I=1}^{n} N_I(x,y)\, \varphi_{pxI}, \\ v_p(x,y,z) &= \sum_{I=1}^{n} N_I(x,y)\, v_{0pI} - z\sum_{I=1}^{n} N_I(x,y)\, \varphi_{pyI}, \\ w_p(x,y) &= \sum_{I=1}^{n} N_I(x,y)\, w_{pI}, \end{aligned} \tag{8}$$

where $\{u_{0pI}, v_{0pI}, w_{pI}, \varphi_{pxI}, \varphi_{pyI}\}^{\mathrm{T}} = \boldsymbol{\delta}_{pI}$ are the nodal parameters of the Ith node of the plate, n is the number of nodes of the plate, φ_{px} and φ_{py} are independent of w_p. Similarly, the displacement field of the x-rib is

$$\begin{aligned} u_{sx}(x,z) &= u_{0s}(x) - z\varphi_{sx}(x) \\ &= \sum_{I=1}^{N} \Phi_{xI}(x)\, u_{0sI} - z\sum_{I=1}^{N} \Phi_{xI}(x)\, \varphi_{sxI}, \\ w_{sx}(x) &= \sum_{I=1}^{N} \Phi_{xI}(x)\, w_{sxI}, \end{aligned} \tag{9}$$

where $\{u_{0sI}, w_{sxI}, \varphi_{sxI}\}^{\mathrm{T}} = \boldsymbol{\delta}_{sxI}$ are the nodal parameters of the x-rib and N is the number of nodes of the x-rib. The shape functions $N_I(x, y)$ and $\Phi_{xI}(x)$ are obtained from (6), and the cubic spline function is used as the weight function.

3.2. A New Transformation Equation of the Nodal Parameters. Along the axis of the x-rib (Figure 1), we take a normal section parallel to z-axis, as shown in Figure 2.

For a node S of the x-rib, there will be a corresponding point P on the plate, and they have the same x and y coordinates. Their displacements follow

$$\left[w_p\right]_P = \left[w_{sx}\right]_S, \tag{10}$$

$$\left[\varphi_{px}\right]_P = \left[\varphi_{sx}\right]_S. \tag{11}$$

And necessarily, at the corresponding point of Node S and Point P in the contact surface between the plate and x-rib, Point C is

$$\left[u_p\right]_C = \left[u_{sx}\right]_C. \tag{12}$$

Remark 1. Point P can be any point on the plate that corresponds to Node S. For every node of the x-rib, a corresponding point on the plate can be found. Similar to the process in [23, 24], the equations that transform the nodal parameters w_{sxI} and φ_{sxI} of the x-rib into the nodal parameters of the plate can be derived as

$$\boldsymbol{\delta}_{sxw} = \mathbf{T}_{sp}\boldsymbol{\delta}_{pw}, \qquad \boldsymbol{\delta}_{sx\varphi} = \mathbf{T}_{sp}\boldsymbol{\delta}_{px\varphi}, \tag{13}$$

where

$$\boldsymbol{\delta}_{sxw} = \{w_{sx1}, w_{sx2}, \ldots, w_{sxN}\}^{\mathrm{T}},$$

$$\mathbf{T}_{sp} = \mathbf{T}_{sx}^{-1}\mathbf{T}_p,$$

$$\mathbf{T}_p = \begin{bmatrix} N_1(x_1, y_1) & N_2(x_1, y_1) & \cdots & N_n(x_1, y_1) \\ N_1(x_2, y_2) & N_2(x_2, y_2) & \cdots & N_n(x_2, y_2) \\ \vdots & \vdots & \ddots & \vdots \\ N_1(x_N, y_N) & N_2(x_N, y_N) & \cdots & N_n(x_N, y_N) \end{bmatrix},$$

$$\boldsymbol{\delta}_{pw} = \left\{w_{p1}, w_{p2}, \ldots, w_{pn}\right\}^{\mathrm{T}},$$

$$\mathbf{T}_{sx} = \begin{bmatrix} \Phi_{x1}(x_1) & \Phi_{x2}(x_1) & \cdots & \Phi_{xN}(x_1) \\ \Phi_{x1}(x_2) & \Phi_{x2}(x_2) & \ldots & \Phi_{xN}(x_2) \\ \vdots & \vdots & \ddots & \vdots \\ \Phi_{x1}(x_N) & \Phi_{x2}(x_N) & \cdots & \Phi_{xN}(x_N) \end{bmatrix},$$

$$\boldsymbol{\delta}_{sxw} = \{w_{sx1}, w_{sx2}, \ldots, w_{sxN}\}^{\mathrm{T}}. \tag{14}$$

$\mathbf{T}_p$ is an $N \times n$ matrix, $\boldsymbol{\delta}_{pw}$ is an $n \times 1$ vector, $\mathbf{T}_{sx}$ is an $N \times N$ square matrix, and $\boldsymbol{\delta}_{sxw}$ is an $N \times 1$ vector. Every row of $\mathbf{T}_p$ and $\mathbf{T}_{sx}$ matrices corresponds to a node of the rib, and, therefore, the matrices have N rows. Equation (12) also gives N equations as

$$\left[u_p\right]_i = \left[u_{sx}\right]_i, \quad (i = 1, 2, \ldots, N), \tag{15}$$

or

$$u_p\left(x_i, y_i, \frac{-h_p}{2}\right) = u_{sx}\left(x_i, \frac{h_{sx}}{2}\right), \quad (i = 1, 2, \ldots, N), \tag{16}$$

where h_p is the thickness of the plate and h_{sx} is the depth of the x-rib. According to the FSDT, (16) can be written as

$$u_{0p}(x_i, y_i) + \frac{h_p}{2}\varphi_{px}(x_i, y_i) = u_{0s}(x_i) - \frac{h_{sx}}{2}\varphi_{sx}(x_i) \quad (i = 1, 2, \ldots, N). \tag{17}$$

And because $\varphi_{px}(x_i, y_i) = \varphi_{sx}(x_i)$ $(i = 1, 2, \ldots, N)$ (11),

$$u_{0p}(x_i, y_i) + \frac{\left(h_p + h_{sx}\right)}{2}\varphi_{px}(x_i, y_i) = u_{0s}(x_i), \quad (i = 1, 2, \ldots, N). \tag{18}$$

The discrete form of (18) is

$$\sum_{I=1}^{n} N_I(x_i, y_i)\, u_{0pI} + es\sum_{I=1}^{n} N_I(x_i, y_i)\, \varphi_{pxI} = \sum_{J=1}^{N} \Phi_{xJ}(x_i)\, u_{0sJ}, \quad (i = 1, 2, \ldots, N) \tag{19}$$

or

$$\mathbf{T}_p\boldsymbol{\delta}_{pu} + es\mathbf{T}_p\boldsymbol{\delta}_{px\varphi} = \mathbf{T}_{sx}\boldsymbol{\delta}_{su}, \tag{20}$$

where $\boldsymbol{\delta}_{pu} = \{u_{0p1}, u_{0p2}, \ldots, u_{0pn}\}^{\mathrm{T}}$, $\boldsymbol{\delta}_{su} = \{u_{0s1}, u_{0s2}, \ldots, u_{0sn}\}^{\mathrm{T}}$, and $es = (h_p + h_{sx})/2$. Equation (20) leads to

$$\boldsymbol{\delta}_{su} = \mathbf{T}_{sx}^{-1}\mathbf{T}_p\boldsymbol{\delta}_{pu} + es\mathbf{T}_{sx}^{-1}\mathbf{T}_p\boldsymbol{\delta}_{px\varphi}. \tag{21}$$

For concentrically ribbed plates, just take $es = 0$. The combination of (13) and (21) gives a new equation that expresses the nodal parameters of the x-rib in terms of the nodal parameters of the plate as follows:

$$\boldsymbol{\delta}_{sx} = \mathbf{T}_{spx}\boldsymbol{\delta}_p, \tag{22}$$

where $\boldsymbol{\delta}_{sx} = \{u_{0s1}, w_{sx1}, \varphi_{sx1}, u_{0s2}, w_{sx2}, \varphi_{sx2}, \ldots, u_{0sN}, w_{sxN}, \varphi_{sxN}\}^{\mathrm{T}}$, $\boldsymbol{\delta}_p = \{u_{0p1}, v_{0p1}, w_{p1}, \varphi_{px1}, \varphi_{py1}, u_{0p2}, v_{0p2}, w_{p2}, \varphi_{px2}, \varphi_{py2}, \ldots, u_{0pn}, v_{0pn}, w_{pn}, \varphi_{pxn}, \varphi_{pyn}\}^{T}$, and $\mathbf{T}_{spx}$ is a $3N \times 5n$ matrix.

With this new transformation equation (22), the meshless model for ribbed plate is more applicable. No matter how the position of ribs changes, we only need to recalculate $\mathbf{T}_p$. Therefore, compared with a finite element model, this meshless model for ribbed plate is expected to have more advantages in future optimization analysis of rib position.

3.3. Strains and Stresses of the Plate and Rib. According to the FSDT and the von Karman theory, the strains of an isotropic plate are

$$\boldsymbol{\varepsilon}_p = \begin{Bmatrix} \varepsilon_x \\ \varepsilon_y \\ \gamma_{xy} \\ \gamma_{xz} \\ \gamma_{yz} \end{Bmatrix} = \begin{Bmatrix} \varepsilon_x^0 \\ \varepsilon_y^0 \\ \gamma_{xy}^0 \\ 0 \\ 0 \end{Bmatrix} + \begin{Bmatrix} -z\varepsilon_x^1 \\ -z\varepsilon_y^1 \\ -z\gamma_{xy}^1 \\ \gamma_{xz}^1 \\ \gamma_{yz}^1 \end{Bmatrix} + \begin{Bmatrix} \varepsilon_x^L \\ \varepsilon_y^L \\ \gamma_{xy}^L \\ 0 \\ 0 \end{Bmatrix}. \tag{23}$$

For convenience, $\boldsymbol{\varepsilon}_p$ is rewritten as

$$\boldsymbol{\varepsilon}_p = \begin{Bmatrix} \varepsilon_x^0 \\ \varepsilon_y^0 \\ \gamma_{xy}^0 \\ 0 \\ 0 \\ 0 \\ 0 \\ 0 \end{Bmatrix} + \begin{Bmatrix} 0 \\ 0 \\ 0 \\ -z\varepsilon_x^1 \\ -z\varepsilon_y^1 \\ -z\gamma_{xy}^1 \\ \gamma_{xz}^1 \\ \gamma_{yz}^1 \end{Bmatrix} + \begin{Bmatrix} \varepsilon_x^L \\ \varepsilon_y^L \\ \gamma_{xy}^L \\ 0 \\ 0 \\ 0 \\ 0 \\ 0 \end{Bmatrix}, \tag{24}$$

where the linear component of the strain includes

$$\begin{Bmatrix} \varepsilon_x^0 \\ \varepsilon_y^0 \\ \gamma_{xy}^0 \end{Bmatrix} = \begin{Bmatrix} u_{0p,x} \\ v_{0p,y} \\ u_{0p,y} + v_{0p,x} \end{Bmatrix} = \sum_{I=1}^{n} \mathbf{B}_{bI}^{e} \boldsymbol{\delta}_{pI},$$

$$\begin{Bmatrix} \varepsilon_x^1 \\ \varepsilon_y^1 \\ \gamma_{xy}^1 \end{Bmatrix} = \begin{Bmatrix} \varphi_{px,x} \\ \varphi_{py,y} \\ \varphi_{px,y} + \varphi_{py,x} \end{Bmatrix} = \sum_{I=1}^{n} \mathbf{B}_{bI}^{b} \boldsymbol{\delta}_{pI}, \tag{25}$$

$$\begin{Bmatrix} \gamma_{xz}^1 \\ \gamma_{yz}^1 \end{Bmatrix} = \begin{Bmatrix} w_{p,x} - \varphi_{px} \\ w_{p,y} - \varphi_{py} \end{Bmatrix} = \sum_{I=1}^{n} \mathbf{B}_{sI} \boldsymbol{\delta}_{pI},$$

where

$$\mathbf{B}_{bI}^{e} = \begin{bmatrix} N_{I,x} & 0 & 0 & 0 & 0 \\ 0 & N_{I,y} & 0 & 0 & 0 \\ N_{I,y} & N_{I,x} & 0 & 0 & 0 \end{bmatrix},$$

$$\mathbf{B}_{bI}^{b} = \begin{bmatrix} 0 & 0 & 0 & N_{I,x} & 0 \\ 0 & 0 & 0 & 0 & N_{I,y} \\ 0 & 0 & 0 & N_{I,y} & N_{I,x} \end{bmatrix}, \tag{26}$$

$$\mathbf{B}_{sI} = \begin{bmatrix} 0 & 0 & N_{I,x} & -N_I & 0 \\ 0 & 0 & N_{I,y} & 0 & -N_I \end{bmatrix}.$$

The nonlinear component of the strain

$$\begin{Bmatrix} \varepsilon_x^L \\ \varepsilon_y^L \\ \gamma_{xy}^L \end{Bmatrix} = \begin{Bmatrix} \frac{1}{2}\left(w_{p,x}\right)^2 \\ \frac{1}{2}\left(w_{p,y}\right)^2 \\ w_{p,x} \cdot w_{p,y} \end{Bmatrix} = \frac{1}{2} \begin{bmatrix} w_{p,x} & 0 \\ 0 & w_{p,y} \\ w_{p,y} & w_{p,x} \end{bmatrix} \begin{Bmatrix} w_{p,x} \\ w_{p,y} \end{Bmatrix} = \frac{1}{2} \mathbf{C} \sum_{I=1}^{n} \mathbf{G}_I \boldsymbol{\delta}_{pI}, \tag{27}$$

where

$$\mathbf{C} = \begin{bmatrix} w_{p,x} & 0 & w_{p,y} \\ 0 & w_{p,y} & w_{p,x} \end{bmatrix}^{\mathrm{T}},$$

$$\mathbf{G}_I = \begin{bmatrix} 0 & 0 & N_{I,x} & 0 & 0 \\ 0 & 0 & N_{I,y} & 0 & 0 \end{bmatrix}. \tag{28}$$

The stress is

$$\boldsymbol{\sigma}_p = \begin{Bmatrix} \sigma_x^0 \\ \sigma_y^0 \\ \tau_{xy}^0 \\ 0 \\ 0 \\ 0 \\ 0 \\ 0 \end{Bmatrix} + \begin{Bmatrix} 0 \\ 0 \\ 0 \\ \sigma_x^1 \\ \sigma_y^1 \\ \tau_{xy}^1 \\ \tau_{xz}^1 \\ \tau_{yz}^1 \end{Bmatrix} + \begin{Bmatrix} \sigma_x^L \\ \sigma_y^L \\ \tau_{xy}^L \\ 0 \\ 0 \\ 0 \\ 0 \\ 0 \end{Bmatrix} = \mathbf{D}_p \boldsymbol{\varepsilon}_p, \tag{29}$$

where

$$\mathbf{D}_p = \begin{bmatrix} \mathbf{D}^e & \mathbf{0} \\ \mathbf{0} & \mathbf{D}^b \end{bmatrix}, \qquad \mathbf{D}^e = \frac{E}{1-\mu^2} \begin{bmatrix} 1 & \mu & 0 \\ \mu & 1 & 0 \\ 0 & 0 & \frac{1-\mu}{2} \end{bmatrix},$$

$$\mathbf{D}^b = \frac{E}{1-\mu^2} \begin{bmatrix} 1 & \mu & 0 & 0 & 0 \\ \mu & 1 & 0 & 0 & 0 \\ 0 & 0 & \frac{1-\mu}{2} & 0 & 0 \\ 0 & 0 & 0 & \frac{1-\mu}{2} & 0 \\ 0 & 0 & 0 & 0 & \frac{1-\mu}{2} \end{bmatrix}. \tag{30}$$

The strain of an isotropic x-rib is

$$\boldsymbol{\varepsilon}_{sx} = \begin{Bmatrix} \varepsilon_{x_{sx}} \\ \gamma_{xz_{sx}} \end{Bmatrix} = \begin{Bmatrix} \varepsilon_{x_{sx}}^0 \\ 0 \end{Bmatrix} + \begin{Bmatrix} -z\varepsilon_{x_{sx}}^1 \\ \gamma_{xz_{sx}}^1 \end{Bmatrix} + \begin{Bmatrix} \varepsilon_{x_{sx}}^L \\ 0 \end{Bmatrix}, \tag{31}$$

which can be rewritten as

$$\boldsymbol{\varepsilon}_{sx} = \begin{Bmatrix} \varepsilon_{x_{sx}}^0 \\ 0 \\ 0 \end{Bmatrix} + \begin{Bmatrix} 0 \\ -z\varepsilon_{x_{sx}}^1 \\ \gamma_{xz_{sx}}^1 \end{Bmatrix} + \begin{Bmatrix} \varepsilon_{x_{sx}}^L \\ 0 \\ 0 \end{Bmatrix}, \tag{32}$$

where the linear component of the strain is

$$\varepsilon_{x_{sx}}^0 = u_{0s,x} = \sum_{I=1}^{N} \mathbf{B}_{sxI}^{e} \boldsymbol{\delta}_{sxI}, \tag{33}$$

$$\varepsilon_{x_{sx}}^1 = \varphi_{sx,x} = \sum_{I=1}^{N} \mathbf{B}_{sxI}^{b} \boldsymbol{\delta}_{sxI}, \tag{34}$$

$$\gamma_{xz_{sx}}^1 = w_{sx,x} - \varphi_{sx} = \sum_{I=1}^{N} \mathbf{B}_{sxsI} \boldsymbol{\delta}_{sxI}, \tag{35}$$

where

$$\mathbf{B}_{sxI}^{e} = \begin{bmatrix} \Phi_{xI,x} & 0 & 0 \end{bmatrix}, \qquad \mathbf{B}_{sxI}^{b} = \begin{bmatrix} 0 & 0 & \Phi_{xI,x} \end{bmatrix},$$
$$\mathbf{B}_{sxsI} = \begin{bmatrix} 0 & \Phi_{xI,x} & -\Phi_{xI} \end{bmatrix}. \tag{36}$$

The nonlinear component of the strain is

$$\varepsilon_{x_{sx}}^L = \frac{1}{2}\left(w_{sx,x}\right)^2 = \frac{1}{2}\left(w_{sx,x}\right) \cdot \left(w_{sx,x}\right) = \frac{1}{2} \mathbf{C}_{sx} \sum_{I=1}^{N} \mathbf{G}_{sxI} \boldsymbol{\delta}_{sxI}, \tag{37}$$

where $\mathbf{C}_{sx} = w_{sx,x}$, $\mathbf{G}_{sxI} = \begin{bmatrix} 0 & \Phi_{xI,x} & 0 \end{bmatrix}$.

The stress is

$$\boldsymbol{\sigma}_{sx} = \begin{Bmatrix} \sigma_{x_{sx}}^0 \\ 0 \\ 0 \end{Bmatrix} + \begin{Bmatrix} 0 \\ \sigma_{x_{sx}}^1 \\ \tau_{xz_{sx}}^1 \end{Bmatrix} + \begin{Bmatrix} \sigma_{x_{sx}}^L \\ 0 \\ 0 \end{Bmatrix} = \begin{Bmatrix} E\varepsilon_{x_{sx}}^0 \\ 0 \\ 0 \end{Bmatrix} + \begin{Bmatrix} 0 \\ -zE\varepsilon_{x_{sx}}^1 \\ \frac{E}{2\left(1+\mu\right)} \gamma_{x_{sx}}^1 \end{Bmatrix} + \begin{Bmatrix} E\varepsilon_{x_{sx}}^L \\ 0 \\ 0 \end{Bmatrix} = \mathbf{D}_{sx} \boldsymbol{\varepsilon}_{sx}, \tag{38}$$

where

$$\mathbf{D}_{sx} = \begin{bmatrix} E & 0 & 0 \\ 0 & E & 0 \\ 0 & 0 & \dfrac{E}{2(1+\mu)} \end{bmatrix}. \tag{39}$$

3.4. Nonlinear Formulations of the Ribbed Plate. The virtual work equation of the ribbed plate is

$$d\boldsymbol{\delta}_p^{\mathrm{T}} \cdot \boldsymbol{\Psi} = \int d\boldsymbol{\varepsilon}_p^{\mathrm{T}} \cdot \boldsymbol{\sigma}_p dv + \int d\boldsymbol{\varepsilon}_{sx}^{\mathrm{T}} \cdot \boldsymbol{\sigma}_{sx} dv - d\boldsymbol{\delta}_p^{\mathrm{T}} \cdot \mathbf{F}_1 = \mathbf{0}, \tag{40}$$

where $\boldsymbol{\Psi}$ is the sum of the internal and external force vectors, $\mathbf{F}_1$ is the sum of all of the loading vectors, $d\boldsymbol{\delta}_p$ is the virtual displacement and $d\boldsymbol{\varepsilon}_p$ is the virtual strain of the plate, and $d\boldsymbol{\varepsilon}_{sx}$ is the virtual strain of the x-rib. We can write the relation between the strain and nodal parameters in an increment form as

$$d\boldsymbol{\varepsilon}_p = \overline{\mathbf{B}} d\boldsymbol{\delta}_p, \tag{41}$$

$$d\boldsymbol{\varepsilon}_{sx} = \overline{\mathbf{B}}_{sx} d\boldsymbol{\delta}_{sx}. \tag{42}$$

Substituting (22) into (42), we have

$$d\boldsymbol{\varepsilon}_{sx} = \overline{\mathbf{B}}_{sx} \mathbf{T}_{spx} d\boldsymbol{\delta}_p. \tag{43}$$

The substitution of (41) and (43) into (40) gives us the nonlinear equilibrium equation of the entire ribbed plate as follows:

$$\boldsymbol{\Psi}(\boldsymbol{\delta}_p) = \int \overline{\mathbf{B}}^{\mathrm{T}} \cdot \boldsymbol{\sigma}_p dv + \int \mathbf{T}_{spx}^{\mathrm{T}} \overline{\mathbf{B}}_{sx}^{\mathrm{T}} \cdot \boldsymbol{\sigma}_{sx} dv - \mathbf{F}_1 = \mathbf{0}, \tag{44}$$

where

$$\overline{\mathbf{B}} = \mathbf{B}_0 + \mathbf{B}_L(\boldsymbol{\delta}_p), \qquad \overline{\mathbf{B}}_{sx} = \mathbf{B}_{0_{sx}} + \mathbf{B}_{L_{sx}}(\boldsymbol{\delta}_{sx}),$$

$$\mathbf{B}_0 = [\mathbf{B}_{01}, \mathbf{B}_{02} \ldots \mathbf{B}_{0n}], \qquad \mathbf{B}_{0I} = \begin{bmatrix} \mathbf{B}_{bI}^e \\ -z\mathbf{B}_{bI}^b \\ \mathbf{B}_{sI} \end{bmatrix}, \tag{45}$$

$$\mathbf{B}_{0_{sx}} = \left[\mathbf{B}_{01_{sx}}, \mathbf{B}_{02_{sx}} \ldots \mathbf{B}_{0N_{sx}}\right], \qquad \mathbf{B}_{0I_{sx}} = \begin{bmatrix} \mathbf{B}_{sxI}^e \\ -z\mathbf{B}_{sxI}^b \\ \mathbf{B}_{sxsI} \end{bmatrix}.$$

$\mathbf{B}_L$ is the function of $\boldsymbol{\delta}_p$, where

$$\mathbf{B}_L = [\mathbf{B}_{L1}, \mathbf{B}_{L2} \ldots \mathbf{B}_{Ln}], \qquad \mathbf{B}_{LI} = \begin{Bmatrix} \mathbf{C} \\ \mathbf{0} \\ \mathbf{0} \end{Bmatrix} \mathbf{G}_I. \tag{46}$$

$\mathbf{B}_{L_{sx}}$ is the function of $\boldsymbol{\delta}_{sx}$, where

$$\mathbf{B}_{L_{sx}} = \left[\mathbf{B}_{L1_{sx}}, \mathbf{B}_{L2_{sx}} \ldots \mathbf{B}_{LN_{sx}}\right], \qquad \mathbf{B}_{LI_{sx}} = \mathbf{C}_{sx}\mathbf{G}_{sxI}. \tag{47}$$

From (44), we have

$$d\boldsymbol{\Psi} = \int d\overline{\mathbf{B}}^{\mathrm{T}} \cdot \boldsymbol{\sigma}_p dv + \int \overline{\mathbf{B}}^{\mathrm{T}} \cdot d\boldsymbol{\sigma}_p dv + \int \mathbf{T}_{spx}^{\mathrm{T}} d\overline{\mathbf{B}}_{sx}^{\mathrm{T}} \cdot \boldsymbol{\sigma}_{sx} dv + \int \mathbf{T}_{spx}^{\mathrm{T}} \overline{\mathbf{B}}_{sx}^{\mathrm{T}} \cdot d\boldsymbol{\sigma}_{sx} dv. \tag{48}$$

Employing (29), (35), (41), and (43), we have

$$d\boldsymbol{\sigma}_p = \mathbf{D}_p d\boldsymbol{\varepsilon}_p = \mathbf{D}_p \overline{\mathbf{B}} d\boldsymbol{\delta}_p, \tag{49}$$

$$d\boldsymbol{\sigma}_{sx} = \mathbf{D}_{sx} d\boldsymbol{\varepsilon}_{sx} = \mathbf{D}_{sx} \overline{\mathbf{B}}_{sx} d\boldsymbol{\delta}_{sx} = \mathbf{D}_{sx} \overline{\mathbf{B}}_{sx} \mathbf{T}_{spx} d\boldsymbol{\delta}_p. \tag{50}$$

Equation (45) gives us

$$d\overline{\mathbf{B}} = d\mathbf{B}_L, \qquad d\overline{\mathbf{B}}_{sx} = d\mathbf{B}_{L_{sx}}. \tag{51}$$

Substituting (49), (50), and (51) into (48), we obtain

$$d\boldsymbol{\Psi} = \int d\mathbf{B}_L^{\mathrm{T}} \cdot \boldsymbol{\sigma}_p dv + \overline{\mathbf{K}} d\boldsymbol{\delta}_p + \int \mathbf{T}_{spx}^{\mathrm{T}} d\mathbf{B}_{L_{sx}}^{\mathrm{T}} \cdot \boldsymbol{\sigma}_{sx} dv + \mathbf{T}_{spx}^{\mathrm{T}} \overline{\mathbf{K}}_{sx} \mathbf{T}_{spx} d\boldsymbol{\delta}_p, \tag{52}$$

where

$$\overline{\mathbf{K}} = \int \overline{\mathbf{B}}^{\mathrm{T}} \mathbf{D}_p \overline{\mathbf{B}} dv = \mathbf{K}_0 + \mathbf{K}_L = \int \mathbf{B}_0^{\mathrm{T}} \mathbf{D}_p \mathbf{B}_0 dv + \int \left(\mathbf{B}_0^{\mathrm{T}} \mathbf{D}_p \mathbf{B}_L + \mathbf{B}_L^{\mathrm{T}} \mathbf{D}_p \mathbf{B}_L + \mathbf{B}_L^{\mathrm{T}} \mathbf{D}_p \mathbf{B}_0\right) dv, \tag{53}$$

$$\int d\mathbf{B}_L^{\mathrm{T}} \cdot \boldsymbol{\sigma}_p dv = \mathbf{K}_\sigma d\boldsymbol{\delta}_p = \left(\int \mathbf{G}^{\mathrm{T}} \mathbf{S} \mathbf{G}\, dv\right) d\boldsymbol{\delta}_p,$$

where

$$\mathbf{G} = [\mathbf{G}_1, \mathbf{G}_2 \ldots \mathbf{G}_n], \qquad \mathbf{S} = \begin{bmatrix} Q_x & Q_{xy} \\ Q_{xy} & Q_y \end{bmatrix}, \qquad \{Q_x \;\; Q_y \;\; Q_{xy}\}^{\mathrm{T}} = \int_{-h_p/2}^{h_p/2} \{\sigma_x \;\; \sigma_y \;\; \tau_{xy}\}^{\mathrm{T}} dz. \tag{54}$$

We can obtain $\overline{\mathbf{K}}_{sx}$ and $\int \mathbf{T}_{spx}^{\mathrm{T}} d\mathbf{B}_{L_{sx}}^{\mathrm{T}} \cdot \boldsymbol{\sigma}_{sx}\, dv$ for x-rib similarly. Therefore, (52) can be written as

$$d\boldsymbol{\Psi} = (\mathbf{K}_0 + \mathbf{K}_\sigma + \mathbf{K}_L) d\boldsymbol{\delta}_p + \mathbf{T}_{spx}^{\mathrm{T}} \left(\mathbf{K}_{0_{sx}} + \mathbf{K}_{\sigma_{sx}} + \mathbf{K}_{L_{sx}}\right) \mathbf{T}_{spx} d\boldsymbol{\delta}_p = \mathbf{K}_T d\boldsymbol{\delta}_p, \tag{55}$$

where

$$\mathbf{K}_T = \mathbf{K}_0 + \mathbf{K}_\sigma + \mathbf{K}_L + \mathbf{T}_{spx}^{\mathrm{T}} \left(\mathbf{K}_{0_{sx}} + \mathbf{K}_{\sigma_{sx}} + \mathbf{K}_{L_{sx}}\right) \mathbf{T}_{spx}. \tag{56}$$

From (44), we obtain

$$\begin{aligned}\boldsymbol{\Psi} &= \int \overline{\mathbf{B}}^{\mathrm{T}} \cdot \boldsymbol{\sigma}_p dv + \int \mathbf{T}_{spx}^{\mathrm{T}} \overline{\mathbf{B}}_{sx}^{\mathrm{T}} \cdot \boldsymbol{\sigma}_{sx} dv - \mathbf{F}_1 \\ &= \int (\mathbf{B}_0 + \mathbf{B}_L) \mathbf{D}_p \left(\mathbf{B}_0 + \frac{1}{2}\mathbf{B}_L\right) dv \boldsymbol{\delta}_p \\ &\quad + \mathbf{T}_{spx}^{\mathrm{T}} \int \left(\mathbf{B}_{0_{sx}} + \mathbf{B}_{L_{sx}}\right) \mathbf{D}_{sx} \left(\mathbf{B}_0 + \frac{1}{2}\mathbf{B}_L\right) dv \mathbf{T}_{spx} \boldsymbol{\delta}_p - \mathbf{F}_1 \\ &= \left(\mathbf{K}_s + \mathbf{T}_{spx}^{\mathrm{T}} \mathbf{K}_{s_{sx}} \mathbf{T}_{spx}\right) \boldsymbol{\delta}_p - \mathbf{F}_1 \\ &= \mathbf{K}_{se} \ \boldsymbol{\delta}_p - \mathbf{F}_1, \end{aligned} \tag{57}$$

where

$$\begin{aligned} \mathbf{K}_{se} &= \mathbf{K}_s + \mathbf{T}_{spx}^{\mathrm{T}} \mathbf{K}_{s_{sx}} \mathbf{T}_{spx}, \\ \mathbf{K}_s &= \int \mathbf{B}_0^{\mathrm{T}} \mathbf{D}_p \mathbf{B}_0 dv + \frac{1}{2} \int \mathbf{B}_0^{\mathrm{T}} \mathbf{D}_p \mathbf{B}_L dv \\ &\quad + \int \mathbf{B}_L^{\mathrm{T}} \mathbf{D}_p \mathbf{B}_0 dv + \frac{1}{2} \int \mathbf{B}_L^{\mathrm{T}} \mathbf{D}_p \mathbf{B}_L dv, \\ \mathbf{K}_{s_{sx}} &= \int \mathbf{B}_{0_{sx}}^{\mathrm{T}} \mathbf{D}_{sx} \mathbf{B}_{0_{sx}} dv + \frac{1}{2} \int \mathbf{B}_{0_{sx}}^{\mathrm{T}} \mathbf{D}_{sx} \mathbf{B}_{L_{sx}} dv \\ &\quad + \int \mathbf{B}_{L_{sx}}^{\mathrm{T}} \mathbf{D}_{sx} \mathbf{B}_{0_{sx}} dv + \frac{1}{2} \int \mathbf{B}_{L_{sx}}^{\mathrm{T}} \mathbf{D}_{sx} \mathbf{B}_{L_{sx}} dv. \end{aligned} \tag{58}$$

3.5. Solution to the Nonlinear Equilibrium Equations. This paper used the Newton-Raphson method to solve nonlinear equilibrium equation (57). The process is as follows.

(1) Take linear solution $\{\boldsymbol{\delta}_p\}_0$ as the first approximated solution $\{\boldsymbol{\delta}_p\}_1$.

(2) Substituting $\{\boldsymbol{\delta}_p\}_1$ into (57) to calculate $\boldsymbol{\Psi}_1$.

(3) Employ (55) to determine $\mathbf{K}_T$.

(4) Obtain the incremental displacements by

$$\Delta\{\boldsymbol{\delta}_p\}_2 = -\mathbf{K}_T^{-1} \boldsymbol{\Psi}_1, \tag{59}$$

and the improved solution

$$\{\boldsymbol{\delta}_p\}_2 = \{\boldsymbol{\delta}_p\}_1 + \Delta\{\boldsymbol{\delta}_p\}_2. \tag{60}$$

(5) Return to step (2) and repeat steps (2) to (5) until $\boldsymbol{\Psi}_n$ is sufficiently small and $\{\boldsymbol{\delta}_p\}_n$ is the final solution.

3.6. Enforcement of Essential Boundary Conditions. Due to a lack of Kronecker delta properties in the shape functions given in (6), it is difficult to impose the essential boundary conditions. The full transformation method that Chen et al. [17] introduced is adopted in this paper to enforce the essential boundary conditions.

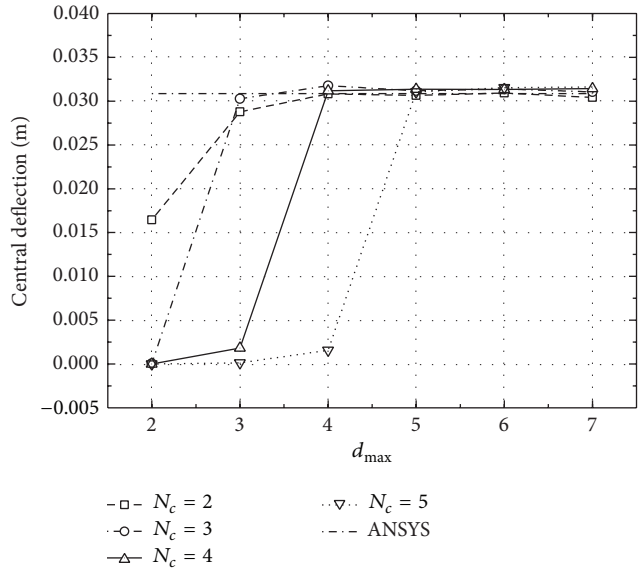

FIGURE 3: Nonlinear deflection of the flat plate under different $d_{\max}$ and N_c.

4. Results and Discussion

4.1. Validation Studies. To show the convergence of the proposed model, and the influences of the support size of the nodes and the order of the basic functions, a clamped square plate subjected to a uniformly distributed pressure of 100 Pa is studied. The width of the plate is 1.8 m, and the thickness is 0.018 m. The Young's modulus of the plate is $E = 3 \times 10^7$ Pa and the Poisson's ratio is $\mu = 0.3$.

The nonlinear deflection of the central point of the plate that is obtained by the proposed model under different support sizes (which are denoted by scaling factors, $d_{\max}$) and different completeness orders of the basic functions N_c is shown in Figure 3, and is compared with the solution that is given by the finite element software, ANSYS, using SHELL63 element.

In this paper, rectangular support is employed, and thus the scaling factors $d_{\max}^x$ and $d_{\max}^y$ are defined by

$$d_{\max}^x = \frac{l_x}{h_{mx}}, \qquad d_{\max}^y = \frac{l_y}{h_{my}}, \tag{61}$$

where l_x, l_y are the lengths of the rectangular support of nodes in the x and y directions, respectively, and h_{mx}, h_{my} are the distances between the two neighboring nodes in the x and y directions, respectively. For convenience, we choose $d_{\max}^x = d_{\max}^y = d_{\max}$. From Figure 3, it can be observed that for a certain meshless scheme (in this case 9×9 nodes) and all of the solutions for different completeness orders (N_c) of the basic functions converge when the support size ($d_{\max}$) is larger than 5. Higher completeness orders (N_c) need a larger support size to make the solution converge.

Secondly, we vary the meshless scheme and obtain the variations of the nonlinear central deflection under certain completeness order of the basic functions (N_c), which are shown in Figures 4, 5, and 6, respectively. The solution that is

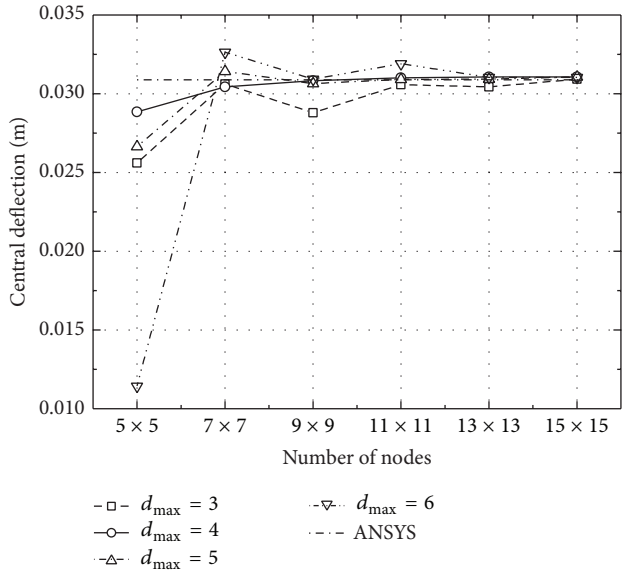

Figure 4: Variation of nonlinear deflection of the flat plate, $N_c = 2$.

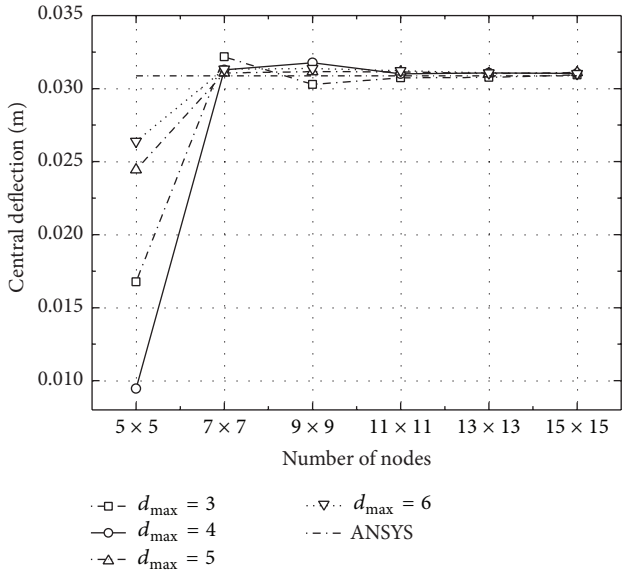

Figure 5: Variation of linear deflection of the flat plate, $N_c = 3$.

given by ANSYS is also in the figures for comparison. Figures 4 to 6 indicate that for certain d_{max}, the solution converges when the number of nodes increases. For certain N_c, the solutions for larger support sizes (d_{max}) converge before those for smaller support sizes do.

From the studies, we find that when the order of basic functions $N_c = 2$ and the support size $d_{max} = 4$ for the plate, the solutions are precise enough with a relatively lower computational cost. A similar convergence study for ribs can be carried out, and the solution given under $N_c = 2$ and the support size $d_{max} = 2$ for the rib is found to be satisfying. Therefore, all of the following examples are calculated with $N_c = 2$, $d_{max} = 4$ (for the plate), and $d_{max} = 2$ (for the ribs).

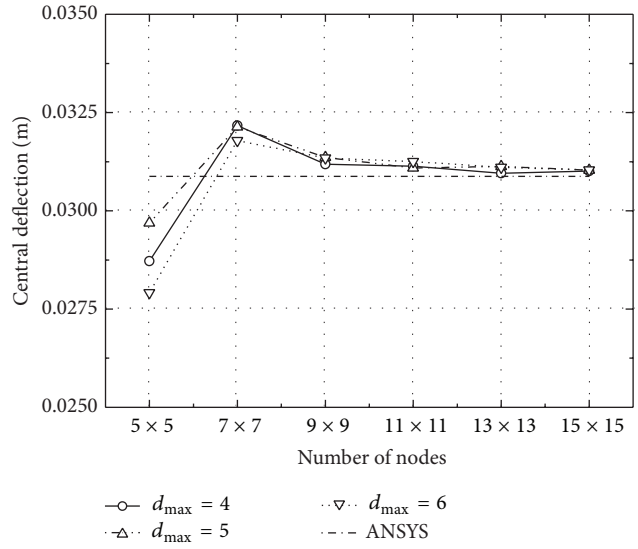

Figure 6: Variation of linear deflection of the flat plate, $N_c = 4$.

Table 1: Central deflection of the rectangular plate with one rib under different loads.

Load (MPa)	Koko and Olson [10] (mm)	Present results (mm)	Relative errors
0.2	5.526	5.31654	3.8%
0.3	7.172	6.9253	3.4%
0.4	8.631	8.47243	1.8%
0.5	9.868	9.82917	0.4%
0.6	11.053	11.0406	0.1%
0.7	11.974	12.1373	−1.4%
0.8	12.961	13.1409	−1.4%

4.2. Rectangular Plate with One Rib. A rectangular plate clamped at two opposite sides and with one rib (Figure 7) located at $x = 500$ mm is studied.

The two other sides of the plate are free. Both the plate and the rib are made of the same material, with Young's modulus $E = 71.7$ GPa and Poisson's ratio $\mu = 0.3$. The plate is under a uniformly distributed load q in the z-direction, and the q ranges from 0.2 to 0.8 MPa. The central deflections of the plate obtained by the proposed model and given by Koko and Olson [10] under different loads are shown in Table 1. The present solution is based on the following discrete scheme: 13×13 for the plate and 13 for the rib.

4.3. Square Plate with Two Cross Ribs. A simply supported square plate with two ribs is studied. The ribs are located at $x = 0.5$ m and $y = 0.5$ m, and they are made of the same material (Figure 8) as the plate.

Young's modulus and Poisson's ratio are $E = 71.7$ GPa and $\mu = 0.33$, respectively. Under a uniformly distributed load q in the z-direction, the load-central deflection curves of the plate given by the proposed model and a large deflection analysis of FEM are shown in Figure 9. When the plate is fully clamped, the load-central stress σ_x curves of the top surface

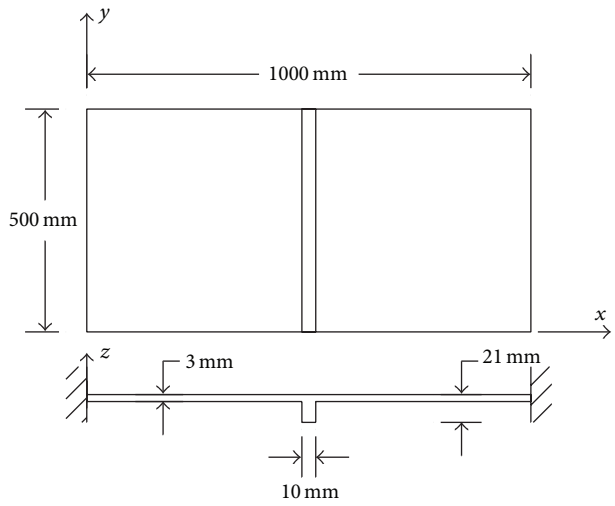

Figure 7: Rectangular plate with one rib.

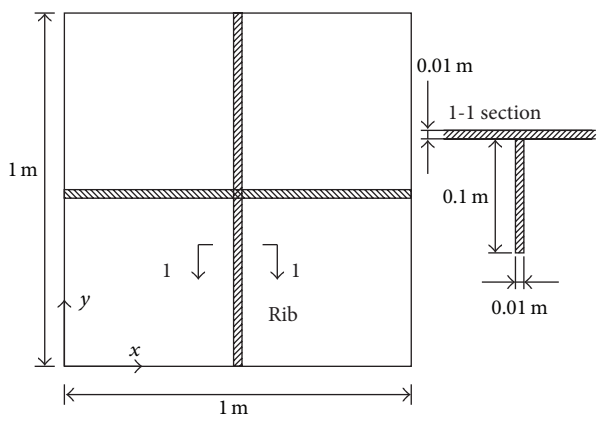

Figure 8: Square plate with two cross ribs.

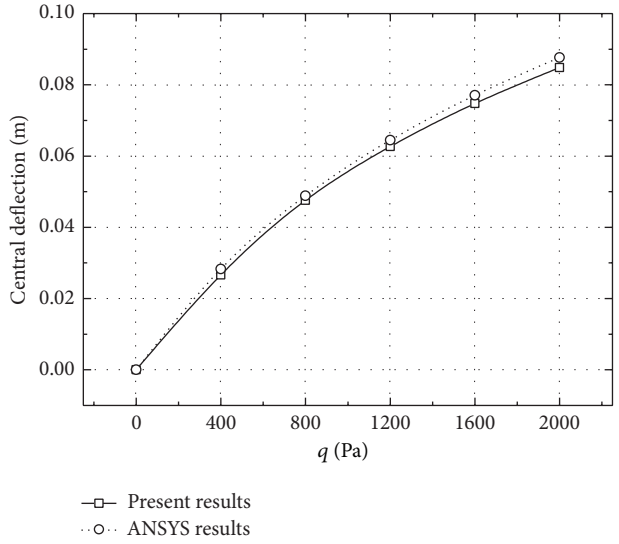

Figure 9: Load-central deflection curve of the simply supported square plate with two ribs.

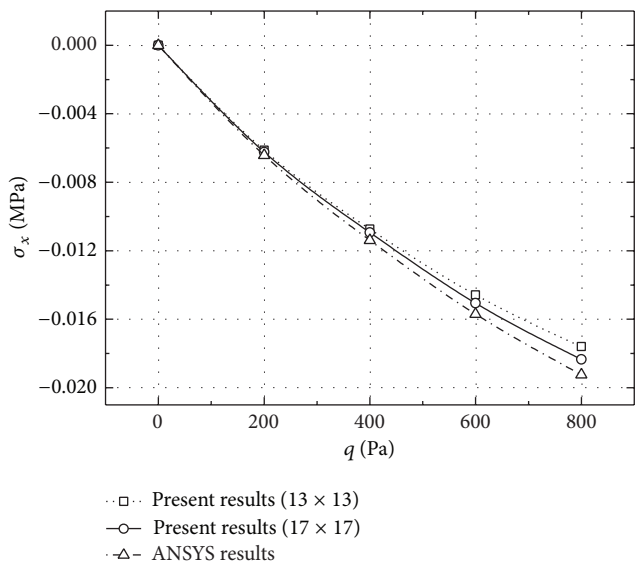

Figure 10: Load-stress curve of the clamped square plate with two ribs.

of the plate are shown in Figure 10. The solution of FEM is obtained using ANSYS software with a three-dimensional model (SOLID45 element is used). The number of discrete elements is 30416 (Figure 11), and two layers are used along the thickness. Figure 9 shows good agreement. In Figure 10, one can observe that the present results given by a discrete scheme of 13×13 nodes have some differences from the results of ANSYS, but the results given by a discrete scheme of 17×17 nodes agree well with the results of ANSYS. It illustrates that the proposed model need more discrete nodes to calculate stress than it need to calculate displacement.

If the thickness of the plate is increased to 0.1 m and the plate is clamped, the load-central deflection curves of the plate are shown in Figure 12.

4.4. Square Plate with One Rib and Different Discretization Schemes. A square plate with one rib located at $x = 0.5$ m (Figure 13) is studied. The rib is made of the same material as the plate. Consider $E = 1.7 \times 10^7$ Pa and $\mu = 0.3$.

The plate is under a uniformly distributed load q that ranges from 0 to 0.1 MPa in the z-direction. To test the new transformation equation (22) that was derived in Section 3.2, the central deflection of the plate is given by ANSYS and the proposed model (with different meshless schemes). In ANSYS, a three-dimensional model for the ribbed plate is used, and the number of discrete elements (SOLID45 element) is 1800 (Figure 14).

Firstly, the present results (Figure 17) are computed using 81 plate nodes (uniform and nonuniform distribution, as shown in Figures 15 and 16, resp.).

Secondly, the present results (Figure 20) are calculated by discretizing the plate with 121 nodes (uniform and nonuniform distribution, as shown in Figures 18 and 19, resp.).

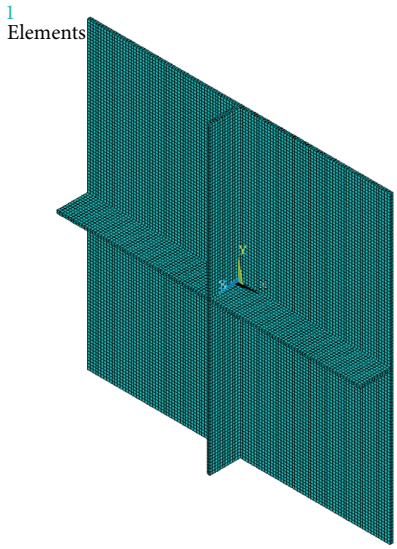

Figure 11: 3D finite element model of a square plate with two ribs.

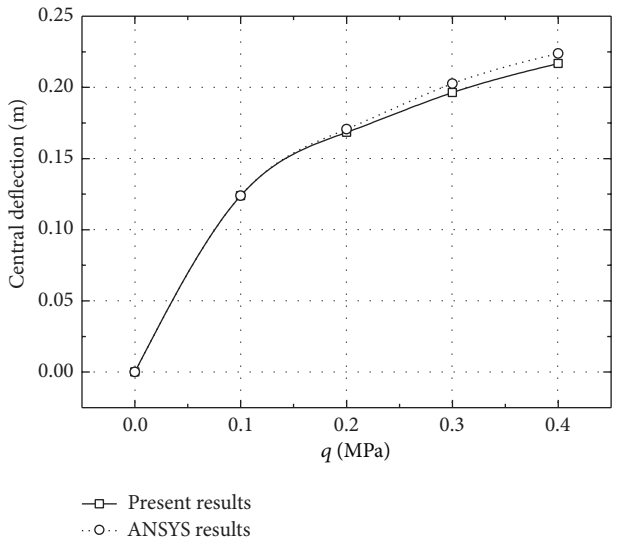

Figure 12: Load-central deflection curve of the clamped square plate with two ribs.

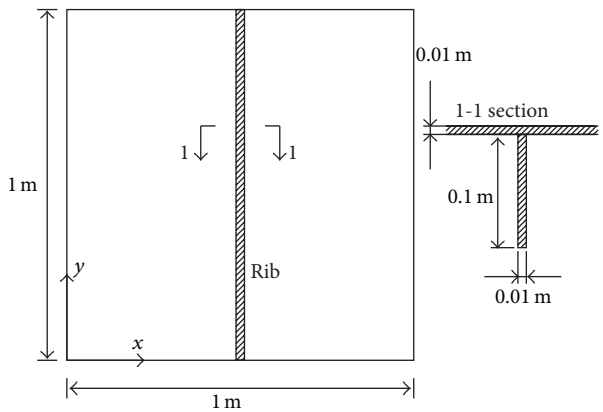

Figure 13: Square plate with one rib.

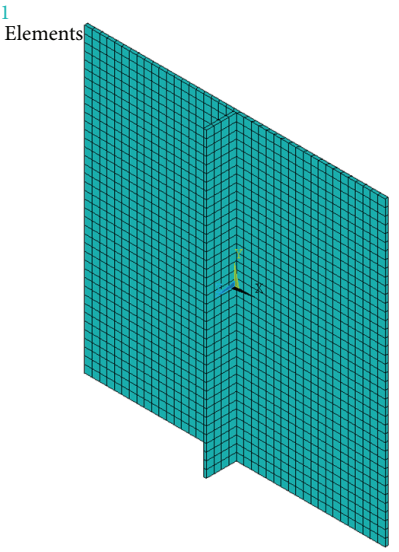

Figure 14: 3D finite element model of a square plate with one rib.

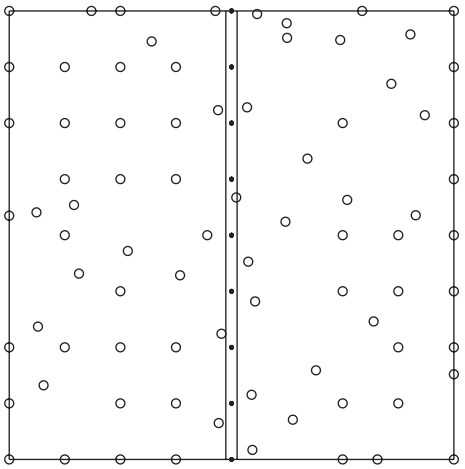

Figure 15: Nonuniform distribution of the 81 plate nodes.

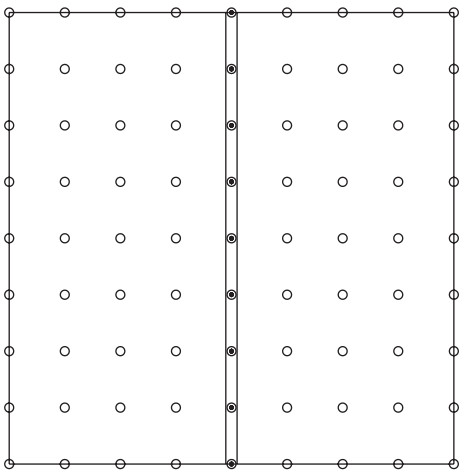

Figure 16: Uniform distribution of the 9 × 9 plate nodes.

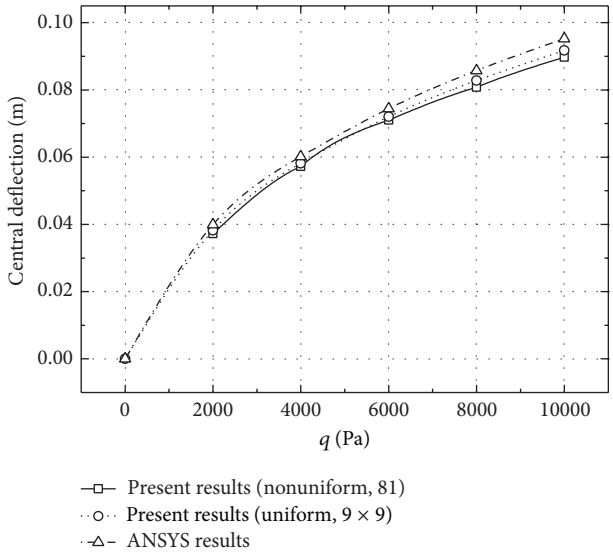

Figure 17: Central deflection of the clamped plate with one rib (81 nodes).

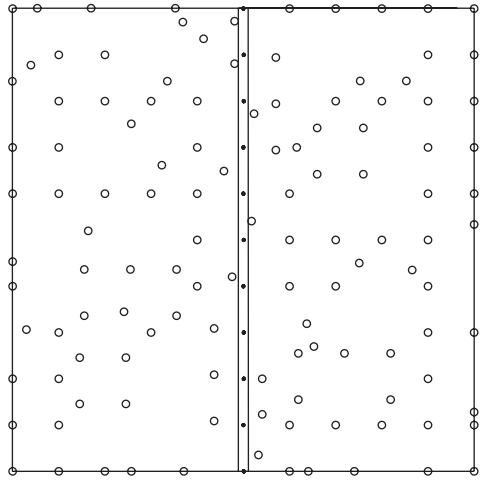

Figure 18: Nonuniform distribution of the 121 plate nodes.

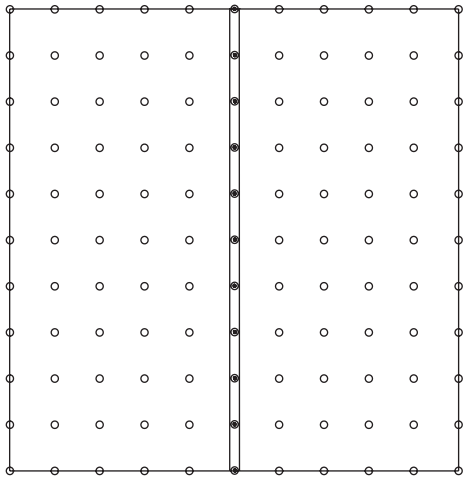

Figure 19: Uniform distribution of the 11 × 11 plate nodes.

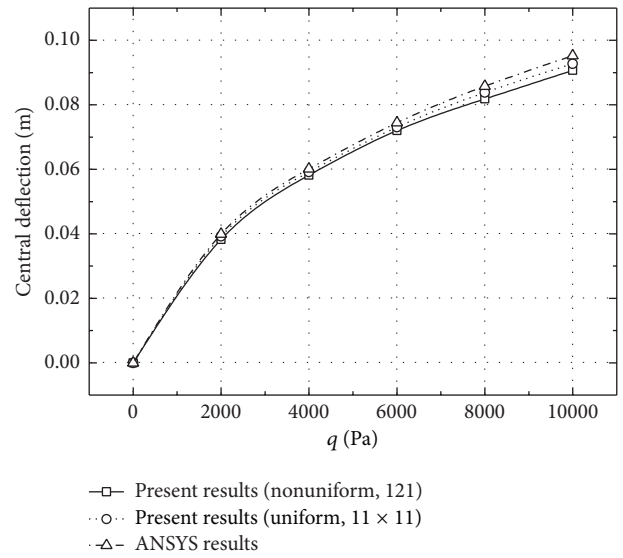

Figure 20: Central deflection of the clamped plate with one rib (121 nodes).

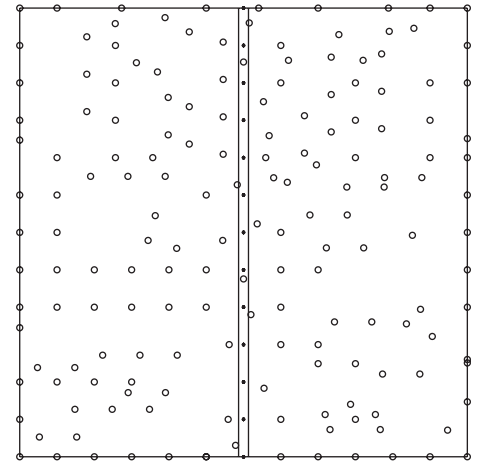

Figure 21: Nonuniform distribution of the 169 plate nodes.

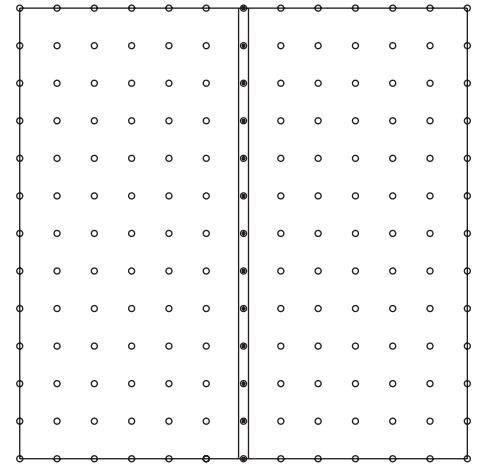

Figure 22: Uniform distribution of the 13 × 13 plate nodes.

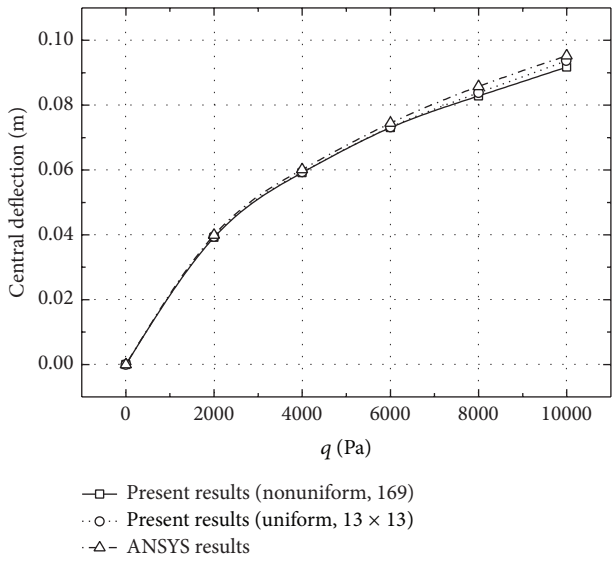

Figure 23: Central deflection of the clamped plate with one rib (169 nodes).

Finally, the present results (Figure 23) are given by a discretization scheme of 169 plate nodes (uniform and nonuniform distribution, as shown in Figures 21 and 22).

In Figures 15, 16, 18, 19, 21, and 22, the small circles represent the nodes of the plate and the black dots denote the nodes of the stiffener. Figures 17, 20, and 23 display clearly that, in the cases of uniform distribution, Point P is taken to be a node of the plate, while, in the cases of nonuniform distribution, Point P is no longer a node of the plate (see Section 3.2). In Figure 17, the agreement is good but slight difference exists. When we increase the nodes of plate, the agreement becomes much better (Figures 20 and 23). The results in Figures 17, 20, and 23 demonstrate that the placement of the plate nodes nearly has no effects on the final solution and prove the accuracy of the new transformation equation (22) that was derived in Section 3.2.

5. Conclusions

This paper presents a meshless model, which is based on the FSDT and the MLS approximation to study the geometric nonlinear behaviors of ribbed plate structures. Considering a ribbed plate as a composite structure of plate and ribs, and starting from the large deflection theory of von Karman, the nonlinear behaviors of the plate and the ribs were studied, respectively. Then, employing the meshless advantages of the proposed model, the nonlinear governing equations of the plate and the ribs were superposed with a new equation derived for the nodal parameter transformation of the plate and the ribs, and the geometric nonlinear equilibrium equation of the entire structure is established. The advantages of the proposed model are that the ribs can be placed anywhere on a plate and any changes of their positions will not lead to the remeshing of the plate, which enhances computational efficiency in solving the optimization of rib layout under the consideration of nonlinear deformation. And the proposed model do not rely on mesh; therefore, mesh disorder due to the large deformation of problem domain is avoided. The present results are compared with those from three-dimensional FEM analysis and pieces of literature. Good agreement can be observed, which proves the accuracy of the proposed meshless model.

Conflict of Interests

The authors declare that there is no conflict of interests regarding the publication of this paper.

Acknowledgments

The work that is described in this paper has been supported by the grants awarded by the National Natural Science Foundation of China (Projects nos. 11102044, 51168003, and 51168005) and the Systematic Project of Guangxi Key Laboratory of Disaster Prevention and Structural Safety (Project no. 2012ZDX07).

References

[1] S. Kendrick, "The analysis of a flat plated grillage," *European Shipbuilding*, vol. 5, pp. 4–10, 1956.

[2] H. A. Schade, "The orthogonally stiffened plate under uniform lateral load," *Journal of Applied Mechanics ASME*, vol. 62, pp. 143–146, 1940.

[3] C. L. Kirk, "Vibration of centrally stiffened rectangular plate," *Journal of the Royal Aeronautical Society*, vol. 65, pp. 695–697, 1961.

[4] K. M. Liew, Y. Xiang, and S. Kitipornchai, "Transverse vibration of thick rectangular plates—III. Effects of multiple eccentric internal ring supports," *Computers and Structures*, vol. 49, no. 1, pp. 59–67, 1993.

[5] K. M. Liew, Y. Xiang, S. Kitipornchai, and M. K. Lim, "Vibration of rectangular Mindlin plates with intermediate stiffeners," *Journal of Vibration and Acoustics*, vol. 116, no. 4, pp. 529–535, 1994.

[6] K. M. Liew, Y. Xiang, S. Kitipornchai, and J. L. Meek, "Formulation of Mindlin-Engesser model for stiffened plate vibration," *Computer Methods in Applied Mechanics and Engineering*, vol. 120, no. 3-4, pp. 339–353, 1995.

[7] Y. Xiang, S. Kitipornchai, K. M. Liew, and M. K. Lim, "Vibration of stiffened skew Mindlin plates," *Acta Mechanica*, vol. 112, no. 1–4, pp. 11–28, 1995.

[8] J. R. O'Leary and I. Harari, "Finite element analysis of stiffened plates," *Computers and Structures*, vol. 21, no. 5, pp. 973–985, 1985.

[9] A. Deb and M. Booton, "Finite element models for stiffened plates under transverse loading," *Computers and Structures*, vol. 28, no. 3, pp. 361–372, 1988.

[10] T. S. Koko and M. D. Olson, "Non-linear analysis of stiffened plates using super elements," *International Journal for Numerical Methods in Engineering*, vol. 31, no. 2, pp. 319–343, 1991.

[11] D. V. Rao, A. H. Sheikh, and M. Mukhopadhyay, "A finite element large displacement analysis of stiffened plates," *Computers and Structures*, vol. 47, no. 6, pp. 987–993, 1993.

[12] B. Chattopadhyay, P. K. Sinha, and M. Mukhopadhyay, "Geometrically nonlinear analysis of composite stiffened plates using finite elements," *Composite Structures*, vol. 31, no. 2, pp. 107–118, 1995.

[13] A. H. Sheikh and M. Mukhopadhyay, "Geometric nonlinear analysis of stiffened plates by the spline finite strip method," *Computers and Structures*, vol. 76, no. 6, pp. 765–785, 2000.

[14] B. Nayroles, G. Touzot, and P. Villon, "Generalizing the finite element method: diffuse approximation and diffuse elements," *Computational Mechanics*, vol. 10, no. 5, pp. 307–318, 1992.

[15] T. Belytschko, Y. Y. Lu, and L. Gu, "Element-free Galerkin methods," *International Journal for Numerical Methods in Engineering*, vol. 37, no. 2, pp. 229–256, 1994.

[16] Y. Cheng and J. Li, "Complex variable meshless method for fracture problems," *Science in China G*, vol. 49, no. 1, pp. 46–59, 2006.

[17] J. S. Chen, C. Pan, C. T. Wu, and W. K. Liu, "Reproducing Kernel Particle Methods for large deformation analysis of nonlinear structures," *Computer Methods in Applied Mechanics and Engineering*, vol. 139, no. 1–4, pp. 195–227, 1996.

[18] M. Peng, P. Liu, and Y. Cheng, "The complex variable element-free Galerkin (CVEFG) method for two-dimensional elasticity problems," *International Journal of Applied Mechanics*, vol. 1, no. 2, pp. 367–385, 2009.

[19] H. Gao and Y. Cheng, "A complex variable meshless manifold method for fracture problems," *International Journal of Computational Methods*, vol. 7, no. 1, pp. 55–81, 2010.

[20] Z. Lei, K. M. Liew, and J. L. Yu, "Buckling analysis of functionally graded carbon nanotube reinforced composite plates using the element-free kp-Ritz method," *Composite Structures*, vol. 98, pp. 160–168, 2013.

[21] Z. Lei, K. M. Liew, and J. L. Yu, "Large deflection analysis of functionally graded carbon nanotube-reinforced composite plates by the element-free kp-Ritz method," *Computer Methods in Applied Mechanics and Engineering*, vol. 256, pp. 189–199, 2013.

[22] L. W. Zhang, P. Zhu, and K. M. Liew, "Thermal buckling of functionally graded plates using a local Kriging meshless method," *Composite Structures*, vol. 108, pp. 472–492, 2014.

[23] L. X. Peng, K. M. Liew, and S. Kitipornchai, "Buckling and free vibration analyses of stiffened plates using the FSDT mesh-free method," *Journal of Sound and Vibration*, vol. 289, no. 3, pp. 421–449, 2006.

[24] L. X. Peng, K. M. Liew, and S. Kitipornchai, "Analysis of stiffened corrugated plates based on the FSDT via the mesh-free method," *International Journal of Mechanical Sciences*, vol. 49, no. 3, pp. 364–378, 2007.

[25] J. N. Reddy, *Theory and Analysis of Elastic Plates*, Taylor & Francis, London, UK, 1999.

[26] K. M. Liew, Y. Xiang, and S. Kitipornchai, "Research on thick plate vibration: a literature survey," *Journal of Sound and Vibration*, vol. 180, no. 1, pp. 163–176, 1995.